Title: Laser powder bed fusion of titanium-tantalum alloys: Compositions and designs for biomedical applications

Authors:

Sheng Huang [a,*], (S. Huang) sheng007@e.ntu.edu.sg

Swee Leong Sing [a,*], (S.L. Sing) sing0011@e.ntu.edu.sg

Geoff Delooze [b], (G. Delooze) geoff.delooze@csiro.au

Robert Wilson [b], (R. Wilson) robert.wilson@csiro.au

Wai Yee Yeong [a], (W.Y. Yeong) wyyeong@ntu.edu.sg +65 6790 4343 (corresponding author)

**these authors contributed equally to this paper*

Affiliations:

[a] Singapore Centre for 3D Printing, School of Mechanical & Aerospace Engineering, Nanyang Technological University

Address: N3.1-B2C-03, 50 Nanyang Avenue, Singapore 639798

[b] Commonwealth Scientific and Industrial Research Organisation

Address: Research Way, Clayton Vic 3168, Australia

Keywords: Additive Manufacturing, 3D Printing, Powder Bed Fusion, Selective Laser Melting, In-situ Alloying, Titanium-tantalum

Abstract:

In this study, laser powder bed fusion (L-PBF), also known as selective laser melting (SLM), was used to fabricate samples of titanium-tantalum (TiTa) alloys with 0, 10, 30 and 50 wt.% of tantalum using in-situ alloying. As-fabricated samples comprised of randomly dispersed pure Ta particles in a titanium-tantalum matrix. Porosity and unmelted Ta particles of the samples were revealed using an optical microscope (OM). The microstructure of the alloys were determined by combination of field emission scanning electron microscopy (FE-SEM), electron back scatter diffraction (EBSD) and X-ray diffraction (XRD). The mechanical properties of the alloys were investigated with tensile test and Vickers hardness test. To ascertain the suitability of these alloys as biomaterials, Ti-50Ta scaffolds with 60% porosity were characterized biologically. This study further shows that porous TiTa scaffolds fabricated using L-PBF are biocompatible with comparable biological results and manufacturability as Ti6Al4V and commercially pure titanium, based on the results obtained from cell culture with human osteosarcoma cell line SAOS-2.

1. Introduction

Laser powder bed fusion (L-PBF), also commonly known as selective laser melting (SLM), additive manufacturing (AM) technique, commonly known as 3D printing. L-PBF uses a laser as the energy source to completely melt and fuse powder materials to directly form parts that can be fully functional. Details of L-PBF have been described in previous works [1-4]. L-PBF has the key advantages of AM, such as having lesser design constraints and allowing complex geometries to be fabricated. This has led to interest in developing this technique for biomedical applications due to the capability in mass customization.

Due to the interest in using L-PBF for biomedical applications, many studies have focused on L-PBF of pure titanium and titanium-based alloys [5-7]. Tantalum is an excellent choice for alloying with titanium for biomedical applications due to its high biocompatibility, corrosion resistance and good mechanical properties. In addition, titanium-tantalum (TiTa) alloys are promising materials for such applications due to high strength to density ratio [8]. Despite the advantages, TiTa alloys are still not widely adopted in applications due to the difficulty in combining these two metals as they have great difference in density and melting point [9]. Density of titanium and tantalum is 4.5 and 16.6 g/cm^3, while melting point of titanium and tantalum is 1670 ^{o}C and 3020 ^{o}C respectively. These large differences could lead to inhomogeneity during the alloy formation as the large difference in density can lead to segregation of elements in the alloys. The high melting point of tantalum may risk the titanium being vaporized during conventional alloying processes that typically melt both materials. The boiling point of titanium is 3287^{o}C, which is very close to the melting point of tantalum. Previous work has shown L-PBF is capable of producing TiTa alloys [10-13], proving the potential for *in situ* alloying and direct fabrication of functional parts .

As L-PBF produced TiTa is new, little is known about the effect of tantalum compositions on the microstructure and mechanical properties of the alloys. The biological response of these materials also needs to be studied to ascertain the suitability of them for biomedical applications. In this paper, the effect of tantalum compositions is studied by characterizing the L-PBF produced samples' microstructure and mechanical properties. Porous lattice structures were produced with Ti50Ta (wt.%) and analyzed biologically. The biological response is benchmarked against the more established Grade 2 commercially pure titanium and Ti6Al4V produced by L-PBF.

2. Experimental details

2.1 Laser powder bed fusion

Samples were fabricated using in-house developed titanium-tantalum powder blends (with 10, 30 and 50 wt.% tantalum). The titanium-tantalum powder blends were obtained from mixing gas atomized commercially pure titanium (CP Ti) and tantalum powders. The CP Ti powder (Grade 2 ASTM B348, LPW Technology Ltd, United Kingdom) particles were spherical with D_{50} of 43.5 μm. The tantalum powder (Singapore Demand Planner Ltd, Singapore) particles were irregular in shape with D_{50} of 44 μm. The two elemental powders were mixed and then spun for 12 h at a rate of 60 rpm using a tumbler mixer (Inversina 2 L, Bioengineering AG).

The fabrication of the samples was carried out using a SLM 250 HL machine (SLM Solutions Group AG), equipped with a fiber laser with a Gaussian bean profile and focus diameter of 80 μm. The maximum laser power is 400 W. All processes were carried out in an argon environment with less than 0.05% oxygen to prevent oxidation and interstitial element

contaminations such as hydrogen and nitrogen pick up during the L-PBF process. All samples were prepared using the same process parameters, hence the same energy density input.

2.2 Metallographic Characterization

The samples were sectioned to reveal the cross-sectional area perpendicular to the build direction. The cross-sections were then ground with grit #320 SiC-paper followed by MD-Largo (DiaPro Largo 9 μm suspension). They were finish polished with MD-Chem (OPS 0.04 μm suspension + H_2O_2) to achieve mirror finish for further analysis.

The polished samples were observed with optical microscope (OM) to reveal the part's quality. Image analysis was done with ImageJ software to obtain the percentage porosity and area percentage of unmelted Ta.

To identify the constituent phases, the polished samples were analyzed with X-ray diffraction (XRD, PANalytical Empyrean, Netherlands) using Cu-Kα radiation and a step size of 0.05°.

Microstructure analysis was done with a field emission scanning electron microscope (FE-SEM, JEOL 7600F, JEOL, Japan) equipped with backscatter electron (BSE) detector. Texture analysis was done with electron backscattering diffraction (EBSD) analysis using FE-SEM equipped with an AZtecHKL Oxford system, scanning with a step size of 0.5 μm.

2.3 Mechanical Characterization

Tensile coupons, based on ASTM E8 sub-size specimen, were produced using electrical discharge machining (EDM) from blocks fabricated by L-PBF. An Instron Static Tester Series 5569, 50 kN machine with a loading rate of 1 mm/min was applied on all tensile samples. Tensile test loading direction was perpendicular to the build direction (z-direction) of the

samples. Average values are derived from the mean of five specimens for each TiTa alloy of a particular tantalum content. Fracture surfaces were observed with FE-SEM under the secondary electron (SE) mode to obtain the fractography.

The microhardness test of the material was carried out using Vickers hardness tester (DuraScan, Struers, Denmark) on the xy- and yz- planes where a load of 100 g and a loading time of 15 s were used. Average values are derived from the mean of 20 indentation on each plane, across five specimens, for each TiTa alloy of a particular tantalum content.

2.4 Biological Characterization

The lattice structures used were designed based on the design constraints obtained from literature [14-17]. The unit cell is made up of horizontal and vertical crosses connected through the origin with 0.285 mm square cross-sectioned struts. The dimensions of the repeating unit cell were 1 mm by 1 mm by 1 mm as shown in Figure 1. The same computer aided design (CAD) file was used for the fabrication of all CP Ti, Ti6Al4V and Ti50Ta samples for the biological characterisation. L-PBF with the same process parameters and conditions is used to fabricate all the samples. The L-PBF capability in building horizontal and vertical struts has been demonstrated in the previous work [18].

The human osteosarcoma cell line SAOS-2, which can be used to study events associated with the late osteoblastic differentiation stage in human cells, was obtained from the American Type Culture Collection (HTB85, American Type Culture Collection, ATCC). The cells were cultured in McCoy's 5A modified medium (16600-082, Gibco, Life Technologies), supplemented with 15 % foetal bovine serum and 1 % antibiotics. The cells were cultured at 37 °C with 5 % CO_2, routinely trypsinized after confluency, counted, and seeded onto the scaffolds. The scaffolds

were sterilized by soaking in 70 % ethanol for an hour and autoclaved for 20 minutes at 121 ^{o}C. A cell suspension of 5×10^3 cells in 100 µL was added onto the top of each scaffold. After initial incubation of 3 hours, 1 mL of culture medium was added to cover the scaffold for cell proliferation.

To determine the biocompatibility of the scaffolds, tests using Quant-iT PicoGreen dsDNA Assay Kit (Life Technologies, Thermo Fisher Scientific) were performed on days 1, 3 and 7. Each material (CP Ti, TiTa and Ti6Al4V) has 3 replicates. Day 7 is the end of the culture period. The amount of double stranded deoxyribonucleic acid (dsDNA) corresponds to the number of SAOS-2 cells found within the scaffolds. One-way analysis of variance (ANOVA) together with Tukey-Kramer post-hoc analysis was used to identify possible significant differences in number of SAOS-2 cells (with significant threshold: $p < 0.05$) between the TiTa, CP Ti and Ti6Al4V.

The cells were also cultured in Dulbecco's Modified Eagle's Medium (DMEM, Gibco, Thermo Fisher Scientific). Cultures were maintained at 37 ^{o}C with 5 % CO_2 in a humidified incubator. Cells were subcultured every two days with 0.01 % trypsin (Gibco, Thermo Fisher Scientific). The lattice structures were sterilized using autoclave and dried in 60 ^{o}C oven overnight. Before cell culturing, the samples were placed in 24-well plates, one in each well and UV sterilised for 15 minutes.

5000 cells were suspended in 100 µL cell culture medium and seeded on the surface of the lattice structures. The seeded samples were transferred into incubation for 1 hour to allow cell adhesion. Then 1 mL of cell culture medium was then added to each well by the wall side without directly flushing the lattice structures surface. Cultures were carried out for 1, 4 and 7 days until stained

with live/dead staining kit (Invitrogen, Thermo Fisher Scientific) for florescent microscopy. Each material (Grade 2 CP Ti, Ti50Ta and Grade 23 Ti6Al4V) has 3 replicates.

3. Results and Discussion

3.1 Quality of titanium-tantalum parts

Table 1 summarizes the percentage porosity and the area percentage of unmelted Ta associated with each L-PBF built TiTa alloys via *in-situ* alloying. With the addition of Ta, an increasing trend of porosity level and the amount of unmelted Ta particles were observed. Nevertheless, a dip of porosity level can be seen as 10 wt% Ta was added into Ti. OM images of polished cross sections revealed possible reason behind such porosity trend (Figure 2). With the addition of Ta, the size of spherical keyhole porosity decreases while the amount of lack-of-fusion defect increases. With constant energy density input, the addition of Ta leads to increased vaporization point and suppressed the formation of keyholes. Meanwhile, the Ta particles can agglomerate and act as heat sink which causes the laser melt pool to freeze before it fuses completely with the previous layer (Figure 5d). The constant energy density input also leads to increasing amount of unmelted Ta particles as Ta (3017 ^{o}C) has much higher melting point as compared to Ti (1668 ^{o}C).

3.2 Microstructures of titanium-tantalum parts

Table 2 summarizes the Ta content in matrix region, the available phase(s) and the mean lath/acicular width within the matrix region associated with each alloy composition in this study. The Ta Content in matrix regions (region away from unmelted Ta particles and Ta depleted area) were identified via EDS analysis. Meanwhile the phase(s) in majority are typed in bold and the phases formation are consistent with past studies on rapidly cooled TiTa alloys [19, 20]. The

conclusion of phase(s) formation is a combined evidence from the XRD analysis, BSE observation and EBSD analysis which will be discussed later in this section. With the BSE and EBSD analysis, the mean lath/acicular width associated with each part at the matrix region were measured and calculated.

Figure 3 illustrates the XRD curves of L-PBF as-built Ti(0, 10, 30, 50)Ta obtained from *in-situ* alloying.

The XRD curve of CP Ti shows the typical hexagonal close packed (HCP) α-Ti peaks. With slight addition of 10 wt.% tantalum, peaks of HCP α' martensite can be observed which is a supersaturated solid solution of β stabilizing elements obtained from a quench-like process. Further addition of tantalum in Ti30Ta leads to peak broadening without obvious peak splitting at the α' peaks. This signifies a mixed HCP α' martensite and orthorhombic α'' martensite formation. Further addition of tantalum leads to the appearance of body centred cubic (BCC) peaks in addition to the α' and α'' martensite(s) peaks in Ti50Ta. The BCC peaks in Ti50Ta are jointly contributed by the un-melted Ta particles as well as the β-Ti phase. The co-existence of Ta particles and β-Ti phase in Ti50Ta are further confirmed with BSE observation (Figure 5d) and EBSD analysis (Figure 6d). It is good to take note that short peaks that coincides with β-Ti peaks indicates the existence of un-melted tantalum in all TiTa alloys in this study.

L-PBF is known to result in high cooling rates (between 10^4 and 10^6 K/s) that forms metastable phases [21-24]. It was well agreed that metastable phases such as (α', α'', ω and metastable β) can exist in rapidly cooled titanium alloy systems [19]. The quench-like process of L-PBF leads to the formation of full α' martensite due to fast cooling from the temperature range of β phase stability. The critical cooling rate necessary for the initiation of the martensitic shear process can

be achieved in the L-PBF process [25]. The α' phase is a supersaturated solid solution of β stabilizing elements in near α Ti composition and can lead to an increase in the α' unit cell volume [19]. Nevertheless, distinguishing XRD peaks between α and α‘ martensite can be difficult as there are only slight differences in their lattice constant. The differences can be shown in α phase [26] and α' martensite [27] of Ti6Al4V alloy, as shown in Table 3. To confirm that the lath phase in the matrix of Ti10Ta is indeed α' phase, line EDS analysis was conducted as shown in Figure 4a. The analysis shows that the lath phase does contains nearly 10 wt% of Ta with no segregation at the lath boundaries, hence confirming it as the α' phase (Figure 4b).

As the composition changes from Ti10Ta to Ti30Ta, the peak broadening effect without obvious peak splitting signifies a transition from α' martensite to α'' martensite. The absence of peak splitting in Ti30Ta is due to the slight changes in lattice structure from α' to α'' martensite(s). The transition of these two martensitic phases is continuous and is often considered as one martensitic phase α'(α'') [28]. The extent of changes in such martensite's lattice structure is highly dependent on the amount of solid solution added [20, 29]. Similar XRD peak broadening effect on TiTa alloys can be observed in past literatures [20, 30].

For Ti50Ta, the addition of tantalum lowers the martensitic finish temperature to below room temperature. Hence, partial martensitic transformation can be observed with the existence of retained prior β phase. The XRD peaks of un-melted tantalum coincides with the peaks of β phase in Ti50Ta, hence body centered cubic (BCC) XRD peaks can be observed in all *in-situ* alloyed parts with tantalum addition [10].

The SEM images illustrated in Figure 5 were taken under the BSE (or SE when specified) mode to reveal parts' microstructure as well as compositional segregation.

Tantalum is a heavier element compared to titanium, which can lead to more back scattering of electrons, hence making BSE imaging mode an effective method to show the compositional contrast in such binary alloys. Figure 5a shows the microstructure of as-built CP Ti in this study which depicts the typical Widmanstätten lath-α microstructure (~ 4.637 μm width) in a L-PBF produced CP Ti part [11, 31]. With slight Ta addition, Ti10Ta shows a finer lath-α' microstructure (~ 3.279 μm width) transformed from prior β phase with cellular sub-structure (Figure 5b). The prior β grain boundaries in Ti10Ta cannot be easily observed from the BSE images and can be better seen from the EBSD mapping (Figure 6b). Both CP Ti (Figure 5a) and Ti10Ta (Figure 5b) parts show occasional microcracks in between the laths with CP Ti showing longer microcracks. It is unclear whether the microcracks are defects inherent of the SLM process or artefacts from the etching effect from the OPS polishing step. Regardless, the highly orientated microcracks from the fractography of CP Ti (Figure 11a) seems to be related to the microcracks as observed in BSE image of CP Ti (Figure 5a). Further addition of tantalum as seen in Ti30Ta leads to substantial formation of Ta poor area (Figure 5c). High magnification BSE images at the matrix region (Figure 5e) of Ti30Ta shows the nanometer sized acicular-α'' structure (~ 0.079 μm width) while the Ta poor region (Figure 5f) shows the lath-α' structure. At Ti50Ta, β phase with cellular sub-structure was stabilized (Figure 5d) which is further confirmed in the EBSD analysis (Figure 6d). A higher magnification of Ti50Ta in the matrix region (Figure 5g) vaguely shows the existence of nanometer scale acicular-α'' structure (~ 0.052 μm width). Similar to Ti30Ta, Ta poor region in the Ti50Ta part shows the formation of lath-α' structure (Figure 5h). In all *in-situ* alloyed TiTa parts, tantalum-rich area (indicated with red arrows in Figure 5) can be seen with some of them surrounded by tantalum depleted area. The tantalum-rich area is caused by incompletely diffused/melted tantalum particles and the frequency of

occurrence increases with more tantalum addition due to the constant energy density input. In Ti50Ta, the BSE image shows a dark tantalum-depleted area surrounding a cluster of agglomerated Ta particles (Figure 5d). The Ta depletion of the area leads to the formation of fine lath-α' martensite which is more obvious in the EBSD-mapping of Ti50Ta represented by overlaid band contrast mapping (Figure 6f). Moreover, the Ta depleted areas are seen to be commonly associated with the lack-of-fusion defect as seen in the overlaid SE image in Figure 5d.

The effect of rapid cooling cycles in L-PBF process is clearly reflected in the microstructure of fabricated parts. The effect of such quench-like process can be seen in BSE images where non-equilibrium elongated phases such as lath-α' (Figure 5f) and acicular-α'' (Figure 5e) were formed. Meanwhile, the formation of cracks between laths might be due to the residual stress from the fast cooling cycle inherent to L-PBF process. The α/α' colony size as well as the width of lath/acicular phase in all the printed parts can be closely associated to the addition of Ta. Ta exhibits slower diffusion rate in high temperature β-Ti as the concentration of Ta increases [32]. Such sluggish diffusion of Ta can become a limiting factor for the growth rate of lath/acicular phase which subsequently leads to finer microstructure [33]. The observed microstructure refinement is consistent with a similar TiTa study previously done [11]. Lath refinement is often related to faster cooling rate in the past [34], but not as suitable as an explanation in this study for the same process parameter has been used for all the studied compositions. With smaller α/α' colonies, the effective slip length will be shorter. A smaller α/α' colony has more resistance towards micro-crack formation as the boundaries and martensitic plates are strong obstacles against microcrack propagation [35]. Rapid solidification can also lead to limited tantalum diffusion, leaving some areas solidified before tantalum has the chance to completely diffuse and

homogenize the area. Hence, most of the tantalum depleted areas can be seen accompanied with some un-melted/incompletely diffused tantalum particles. Such compositional segregation can lead to formation of different phases in different areas, in which the effect is especially prominent in Ti50Ta. Such compositional segregation of tantalum leads to the formation of α' martensite due to insufficient β-stabilizing element to supress such β → α' transformation. With the addition of Ta while maintaining constant energy density input, big cluster of Ta particles in the laser melt pool act as a heat sink which causes premature solidification. The early solidification prevents a good bonding between portion of the melt pool with previously built layer, hence the formation of lack-of-fusion defect.

The formation of cellular substructure can be seen in parts with addition of tantalum and can be related to the planar interface breakdown condition as shown in Equation (1).

$$\frac{G}{R} < \frac{T_{eq}}{D_L} \qquad \text{Equation (1)}$$

where R is the solid growth rate, G is the temperature gradient ahead of solidification front, T_{eq} is the equilibrium solidification range of the alloy and D_L is the solute diffusivity in the liquid [36].

During the solidification process of TiTa alloys, titanium rejection by the solid into the liquid ahead of solidification front occurs and the titanium needs to be transported away from the interface. This leads to a compositional gradient ahead of the solidification front which translates to a variation of liquidus temperature. Depending on the G/R ratio, substructure morphology can go from planar, cellular, columnar dendritic to equiaxed dentritic. If the $\frac{G}{R} > \frac{T_{eq}}{D_L}$, the cellular solidification front can be simply re-melted leading to stabilization of the planar interface. The formation of cellular substructure of TiTa parts in this study can be ascribed to the satisfaction of

$\frac{G}{R} < \frac{T_{eq}}{D_L}$ condition. This leads to the breakdown of a planar interface, resulting in constitutional supercooling and the formation of cellular substructure. In dilute titanium alloys (Figure 5a), there is subtle difference between the solidus and liquidus line and T_{eq} approaches 0. Furthermore, the temperature gradient is positive towards the build direction in a SLM process where $\frac{G}{R} > 0$ [37]. The stable planar interface can be formed in this case without existence of constitutional supercooling, hence the absence of cellular substructure.

Figure 6 elucidates the EBSD mapping of each samples in inverse pole figure - Z (IPF-Z) colouring. Band contrast (BC) mappings are overlaid in some images to show minor phase(s) present in the mapping. Despite being a BSE image, Figure 6e is included to show columnar prior-β grain boundaries associated with Figure 6a.

CP Ti is IPF coloured for HCP indexing (Figure 6a), Ti10Ta for HCP indexing (Figure 6b), Ti30Ta for orthorhombic (Figure 6(c)) and Ti50Ta for a BCC lattice indexing (Figure 6(d)). The band contrast was overlaid on the mapping to show un-melted tantalum in as-built Ti10Ta and Ti30Ta while showing lath-α' in as-printed Ti50Ta. Large amounts of black coloured unindexed area can be seen in the EBSD mapping of Ti30Ta (Figure 6c) and Ti50Ta (Figure 6d) due to the compositional segregation that causes phase differences as well as continuous changes in lattice constant. EBSD mapping of CP Ti (Figure 6a) clearly shows different variants of lath-α nucleated from prior β grains. Unfortunately, the prior β grain boundaries in CP Ti cannot be clearly observed in the EBSD mapping. With the aid of BSE image (Figure 6e), long and large columnar prior β grains in which the lath-α nucleates from can be seen. Nevertheless Ti10Ta (Figure 6b) shows finer lath-α' transformed from columnar prior β along with some stray prior β grains. Meanwhile Ti30Ta (Figure 6c) shows orthorhombic phase with more randomly orientated

elongated prior β grains. Mapping of Ti50Ta shows equiaxed β phase (Figure 6d) as well as lath-α' phase (Figure 6f) surrounding areas with un-melted tantalum due to insufficient tantalum to retain the β phase. The speckles of unindexed area of Ti50Ta within the β phase might be caused by the embedded acicular-α'' phase which is difficult to be indexed (Figure 6f).

Pole figures were plotted to highlight the effect of Ta addition towards the overall parts' texture, as shown in Figure 7.

Burger's orientation relationship of β phase with other phases are listed below to provide a better idea on texture of β grain prior to transformation to a stable/meta-stable phases at room temperature:

$(0001)\alpha \parallel (011)\beta$ [26]

$(001)\alpha' \parallel (011)\beta$ [27]

$(001)\alpha'' \parallel (011)\beta$ [26]

The minimum and maximum value in the pole figures represent the "multiple of uniform density" (MUD) value which can be defined as the intensity of crystallographic orientation with relation to the normalized value in random orientation. The pole figure of CP Ti shows a highly columnar prior β texture that has the axis of (001) plane strongly aligned with the build direction. The pole figure obtained for the as-built titanium is similar to the titanium that undergoes unidirectional rolling above β transus temperature [35]. The maximum MUD value for Ti10Ta (9.81) becomes weaker compared to CP Ti (16.39) but still exhibits columnar prior β characteristics. The pole figure for Ti30Ta shows a more randomly orientated prior β texture compared to Ti10Ta. Nevertheless, preferential prior β grain growth in the (001) direction can

still be seen along the build direction. As-built Ti50Ta shows the weakest texture among all the printed samples. The maximum MUD value is the lowest among all samples (5.44) with the β phase having slight preferential (001) growth in the build direction. The general trend of texture with tantalum addition can be clearly depicted with the MUD value associated with each part (Figure 7).

The crystal nucleation mechanism of an alloy can greatly influence the resultant texture. SLM process typically possesses high *G*/*R* ratio that promotes epitaxial growth (heterogenous nucleation) from the previously formed crystal. Moreover, the general direction of heat flow is opposite to the build direction and promotes competitive growth of crystals. Hence, SLM processed titanium alloys typically possess long columnar prior β grains with respect to the build direction [38]. The addition of tantalum can limit the columnar prior β grain formation by acting as nucleation sites if the tantalum particles do not melt completely before the part solidifies. The promotion of epitaxial growth of prior β crystals from un-melted tantalum particles can occur due to the low lattice mismatch between the two phases. A BSE image of Ti50Ta in the matrix region (Figure 8) clearly shows nucleation of β grain from an un-melted Ta particle. With the un-melted Ta acting as a heat sink, β-Ti "stray" grain can nucleate and grow away from the Ta particles. With the existence of such "stray" grain, columnar β grain parallel to the Z direction will be fully/partially blocked. This results in more grains of different orientations to grow epitaxially from, leading to smaller prior β grains. As more tantalum were added while retaining the same energy density used during SLM, more un-melted tantalum particles are retained and disrupt the formation of columnar grains. Hence, the texture of β/prior β phase becomes weaker as more tantalum particles are added.

3.3 Mechanical properties of titanium-tantalum parts

The tensile properties of L-PBF produced TiTa alloys are shown in Figure 9.

With the addition of Ta, the yield strength (YS) and ultimate tensile strength (UTS) increases and peak at Ti30Ta which immediately followed by a slight drop at Ti50Ta. An inverse trend is observed for the Young's modulus where Ti30Ta exhibits the lowest average value. Such trend is similar to the trend reported in a previous work [39]. The strengthening of the TiTa alloy systems up to Ti30Ta can be caused by a combination of (a) Solid solution strengthening (b) Lattice transformation and (c) Grain boundary strengthening - Hall Petch effect. From the BSE and EBSD analysis, it can be observed that the average value of lath/acicular size decreases with the addition of Ta (Table 2). As the microstructure becomes finer, dislocation movement across the grain boundary can become difficult and thus increases the mechanical strength (Hall Petch effect). The slight drop of strength at Ti50Ta is caused by the formation of β (BCC) phase which exhibits more slip systems. Unlike other TiTa compositions, Ti50Ta has large retained β grains as the majority phase according to the EBSD analysis (Figure 6d). As such, the strengthening effect from lath/acicular refinement is not as effective for Ti50Ta as compared to those in CP Ti, Ti10Ta and Ti30Ta where the lath/acicular phase forms the phase majority. It can be seen that the trend of YS and UTS is closely followed by the trend of microhardness value tested in either the xy- and yz- planes (Figure 10).

The fractography of the TiTa alloys are shown in Figure 11.

All four groups of specimens show signs of ductility as the specimens showed necking before the specimen fractured. The fractographies obtained from SEM confirm that they exhibit both brittle and ductile fracture. The surfaces of the specimens show the presence of cleavage facets that indicates brittle failure, and ductile dimples and voids that indicates ductile fracture. From the

fractography, preferential crack path behaviors can be observed in CP Ti (Figure 11a) which can be correlated with those in Figure 5a. Meanwhile, the fractographies (Figure 11a-d) show that the void occurrence on the fracture surfaces increase with Ta addition which is closely related to the porosity level and the amount of unmelted Ta (Table 1). As observed in the BSE images in Figure 5, unmelted Ta is commonly surrounded by Ta poor region which is comprised of lath-α' phase. Strain incompatibility and stress concentration can be expected at the lath-α'(HCP)/Ta(BCC) boundary due to the lattice mismatch between the two phases [40]. Such mismatch possibly leads to interface rupture and subsequently contribute to void formation and coalescence. Hence, the addition of Ta showed decreasing trend of elongation due to the occurrence of defects such as porosity and unmelted Ta particles. Similar observation was indeed observed in a study on SLM in-situ alloyed Ti-Nb-Sn [41]. Nevertheless, such claim of voids formation remains a sound hypothesis and the fractography only provides indirect evidence. Further investigation is still required to study and confirm such claim of void formation mechanism.

3.4 Biocompatibility Evaluation of Titanium-Tantalum Structures

For the biocompatibility tests, the overall dimensions of the Ti50Ta lattice structures used are 10 mm in diameter and 2 mm in height. The generated CAD model and the as-fabricated L-PBF sample are shown in Figure 12.

Cell viability is assessed using dsDNA picogreen assay. The results are shown in Figure 13.

dsDNA measurements show an increasing trend for all three materials (n = 5) as shown by the red dotted line in Figure 13. After 7 days of *in vitro* culture, the SAOS-2 cells are found to be viable and proliferating on all the scaffolds. On day 1, 3 and 7, the relative cell number on the

scaffolds of the three materials are similar. Using ANOVA, it is statistically determined that there is no significant difference between the results for all three materials on all the 3 time points. However, the insignificant difference in results can be attributed to the slight difference in porosity of the scaffolds due to the L-PBF process. The porosities of the scaffolds are measured and shown in Table 4.

The higher porosity allows more cell growth into the samples along the struts and better nutrient delivery and waste removal for cells that have migrated into the scaffolds [42, 43]. This factor becomes more critical as the number of days of *in vitro* testing increases.

The cells were stained with live/dead kit where live cells will show green florescence, dead cells will show red florescence. Through 7 days of cell culture, very few dead cells were observed as shown in Figure 14. This demonstrates good cell viability in all three materials. However, different cell proliferation rates were observed.

In CP Ti and Ti6Al4V, cells were nearly 80 to 90 % confluent at day 4 and fully confluent at day 7. In contrast, in TiTa, cells were covering less than 50 % of the surface on day 4. However, they were continuously proliferating and became fully confluent at day 7. This trend is also observed in the dsDNA measurements.

Despite the same CAD model used for fabrication of the lattice structures from the three materials, the struts surface roughness can be different. Struts surface roughness is affected by the L-PBF process parameters and material properties [18, 44, 45]. It is well established that surface roughness affects important cell processes such as cell proliferation [46]. It has also been found that increasing roughness on lattice structure surfaces increases alkaline phosphatase (ALP) activity [47]. Hence, the difference in cell proliferation rates may be attributed to the

different struts surface roughness of the lattice structures and varying material surface properties [48]. This will be studied in the future.

4. Conclusion

This study shows that the amount of tantalum in TiTa alloys fabricated using L-PBF has effect on their microstructure and mechanical properties. In addition, porous Ti50Ta scaffolds fabricated using L-PBF are biocompatible. When benchmarked with CP Ti and Ti6Al4V, the Ti50Ta scaffolds show comparable biological results.

Based on the results, the key findings can be summarised:

1) As the content of tantalum increases in the TiTa alloys, the phases present in the alloys change from **α → α' → α"** + α' **→ β + α"** + α'. Phases detected in the alloy matrix are in bold text.

2) Ti30Ta provides the optimal mechanical properties for orthopaedic applications due to its lowest modulus while having the highest UTS and YS. The addition of Ta refines the lath/acicular phase size which strengthens the TiTa alloy up to Ti30Ta. Further Ta addition to Ti50Ta leads course β phase retention.

3) The decrease in elongation to failure with Ta addition is due to the increased amount of porosity and unmelted Ta in the alloy matrix.

4) TiTa scaffolds showed similar biological response as CP Ti and Ti6Al4V, making it a potential novel biocompatible material for biomedical applications.

In vitro experiments in a static environment have been carried out in this study. Further biological response can be obtained using an apatite forming ability test, cytotoxicity test and

measuring the alkaline phosphatase activity. Dynamic environment can also be used as the behaviour of seeded cells on scaffolds is expected to be different in static and dynamic environments. Histological studies can be carried to investigate the path taken by the cells *in vitro* to go into the depth of the lattice structures. *In vivo* tests in animal models can then be carried out with histological type works which will be useful in studying the cells and tissues attachment to the TiTa lattice structures.

ACKNOWLEDGEMENTS

This research is supported by the National Research Foundation, Prime Minister's Office, Singapore under its Medium-Sized Centre funding scheme and the NTU-CSIRO Seed Fund.

REFERENCES

1. Sing, S.L., et al., *Direct selective laser sintering and melting of ceramics: a review.* Rapid Prototyping Journal, 2017. **23**(3): p. 611-623.
2. Yap, C.Y., et al., *Review of selective laser melting: Materials and applications.* Applied Physics Reviews, 2015. **2**(4): p. 041101.
3. Tan, J.H.K., S.L. Sing, and W.Y. Yeong, *Microstructure modelling for metallic additive manufacturing: a review.* Virtual and Physical Prototyping, 2020. **15**(1): p. 87-105.
4. Salmi, A. and E. Atzeni, *Residual stress analysis of thin AlSi10Mg parts produced by Laser Powder Bed Fusion.* Virtual and Physical Prototyping, 2020. **15**(1): p. 49-61.
5. Khorasani, A., et al., *Production of Ti-6Al-4V acetabular shell using selective laser melting: possible limitations in fabrication.* Rapid Prototyping Journal, 2017. **23**(1): p. 110-121.

6. Kang, N., et al., *On the texture, phase and tensile properties of commerically pure Ti produced via selective laer melting assisted by static magnetic field.* Materials Science and Engineering: C, 2017. **70**(1): p. 405-407.

7. Do, D.K. and P. Li, *The effect of laser energy input on the microstructure, physical and mechanical properties of Ti-6Al-4V alloys by selective laser melting.* Virtual and Physical Prototyping, 2016. **11**(1): p. 41-47.

8. de Souza, K.A. and A. Robin, *Preparation and characterization of Ti-Ta alloys for application in corrsive media.* Materials Letters, 2003. **57**: p. 3010-3016.

9. Morita, A., et al., *Alloying titanium and tantalum by cold crucible levitation melting (CCLM) furnace.* Materials Science and Engineering: A, 2000. **280**: p. 208-213.

10. Sing, S.L., W.Y. Yeong, and F.E. Wiria, *Selective laser melting of titanium alloy with 50 wt% tantalum: Microstructure and mechanical properties.* Journal of Alloys and Compounds, 2016. **660**: p. 461-470.

11. Zhao, D., et al., *Improvement on mechanical properties and corrosion resistance of titanium-tantalum alloys in-situ fabricated via selective laser melting.* Journal of Alloys and Compounds, 2019. **804**: p. 288-298.

12. Soro, N., et al., *Evaluation of the mechanical compatibility of additively manufactured porous Ti–25Ta alloy for load-bearing implant applications.* Journal of the Mechanical Behavior of Biomedical Materials, 2019. **97**: p. 149-158.

13. Sing, S.L., F.E. Wiria, and W.Y. Yeong, *Selective laser melting of titanium alloy with 50 wt% tantalum: Effect of laser process parameters on part quality.* International Journal of Refractory Metals and Hard Materials, 2018. **77**: p. 120-127.

14. Barbas, A., et al., *Development and mechanical characterization of porous titanium bone substitutes.* Journal of the Mechanical Behavior of Biomedical Materials, 2012. **9**: p. 34-44.

15. Fukuda, A., et al., *Osteoinduction of porous Ti implants with a channel structure fabricated by selective laser melting.* Acta Biomaterialia, 2011. **7**(5): p. 2327-2336.

16. Mullen, L., et al., *Selective Laser Melting: a regular unit cell approach for the manufacture of porous, titanium, bone in-growth constructs, suitable for orthopedic applications.* Journal of Biomedical Materials Research Part B: Applied Biomaterials, 2009. **89**(2): p. 325-334.

17. Mullen, L., et al., *Selective laser melting: a unit cell approach for the manufacture of porous, titanium, bone in-growth constructs, suitable for orthopedic applications. II. Randomized structures.* Journal of Biomedical Materials Research Part B: Applied Biomaterials, 2010. **92**(1): p. 178-88.

18. Sing, S.L., F.E. Wiria, and W.Y. Yeong, *Selective laser melting of lattice structures: A statistical approach to manufacturability and mechanical behavior*. Robotics and Computer-Integrated Manufacturing, 2018. **49**: p. 170-180.

19. Zhou, Y.L., M. Niinomi, and T. Akahori, *Effects of Ta content on Young's modulus and tensile properties of binary Ti–Ta alloys for biomedical applications.* Materials Science and Engineering: A, 2004. **371**(1): p. 283-290.

20. Dobromyslov, A., et al., *Phase and structural transformations in Ti-Ta alloys.* The Physics of Metals and Metallography, 2009. **107**(5): p. 502-510.

21. Sun, Z., et al., *Selective laser melting of stainless steel 316L with low porosity and high build rates.* Materials & Design, 2016. **104**: p. 197-204.

22. Qiu, C., et al., *A comprehensive study on microstructure and tensile behaviour of a selectively laser melted stainless steel*. Scientific Reports, 2018. **8**(1): p. 7785.

23. Kuo, C.N., et al., *Microstructure evolution and mechanical property response via 3D printing parameter development of Al–Sc alloy*. Virtual and Physical Prototyping, 2020. **15**(1): p. 120-129.

24. Yu, W.H., et al., *Particle-Reinforced Metal Matrix Nanocomposites Fabricated by Selective Laser Melting: A State of the Art Review*. Progress in Materials Science, 2019. **104**: p. 330-379.

25. Motyka, M., et al., *2.02 - Phase Transformations and Characterization of α + β Titanium Alloys*, in *Comprehensive Materials Processing*, S. Hashmi, et al., Editors. 2014, Elsevier: Oxford. p. 7-36.

26. Mantani, Y., et al., *Phase Transformation of α'' Martensite Structure by Aging in Ti-8 mass%Mo Alloy*. Journal of the Japan Institute of Metals and Materials, 2005. **69**(4): p. 385-391.

27. Kazantseva, N., et al., *Martensitic transformations in Ti-6Al-4V (ELI) alloy manufactured by 3D Printing*. Materials Characterization, 2018. **146**: p. 101-112.

28. Bylica, A. and J. Sieniawski, *Titanium and its alloys*. PWN, Warsaw, 1985.

29. Bywater, K. and J. Christian, *Martensitic transformations in titanium-tantalum alloys*. Philosophical Magazine, 1972. **25**(6): p. 1249-1273.

30. Matsumoto, H., et al., *Microstructure and Mechanical Properties of α' Martensite Type Ti Alloys Deformed under the α' Processing*. MATERIALS TRANSACTIONS, 2009. **50**(12): p. 2744-2750.

31. Barriobero-Vila, P., et al., *Peritectic titanium alloys for 3D printing.* Nature Communications, 2018. **9**(1): p. 3426.

32. Ansel, D., et al., *Interdiffusion in the body cubic centeredβ-phase of Ta–Ti alloys.* Acta Materialia, 1998. **46**(2): p. 423-430.

33. Ackerman, A.K., et al., *The Kinetics of Primary Alpha Plate Growth in Titanium Alloys.* arXiv preprint arXiv:1805.09885, 2018.

34. Gil, F.J., et al., *Formation of α-Widmanstätten structure: effects of grain size and cooling rate on the Widmanstätten morphologies and on the mechanical properties in Ti6Al4V alloy.* Journal of Alloys and Compounds, 2001. **329**(1): p. 142-152.

35. Lütjering, G., J. Williams, and A. Gysler, *Microstructure and mechanical properties of titanium alloys*, in *Microstructure And Properties Of Materials: (Volume 2)*. 2000. p. 1-77.

36. DuPont, J.N., *Fundamentals of Weld Solidification*, in *Welding Fundamentals and Processes*, T. Lienert, et al., Editors. 2011, ASM International. p. 0.

37. Thijs, L., et al., *A study of the microstructural evolution during selective laser melting of Ti–6Al–4V.* Acta Materialia, 2010. **58**(9): p. 3303-3312.

38. Mertens, A., et al., *Mechanical properties of alloy Ti–6Al–4V and of stainless steel 316L processed by selective laser melting: influence of out-of-equilibrium microstructures.* Powder Metallurgy, 2014. **57**(3): p. 184-189.

39. Zhou, Y.L., et al., *Comparison of Various Properties between Titanium-Tantalum Alloy and Pure Titanium for Biomedical Applications.* Materials Transactions, 2007. **48**(3): p. 380-384.

40. Zafari, A. and K. Xia, *High Ductility in a fully martensitic microstructure: a paradox in a Ti alloy produced by selective laser melting.* Materials Research Letters, 2018. **6**(11): p. 627-633.

41. Chen, W., et al., *Controlling the microstructure and mechanical properties of a metastable β titanium alloy by selective laser melting.* Materials Science and Engineering: A, 2018. **726**: p. 240-250.

42. Haslauer, C.M., et al., *In vitro biocompatilibity of titanium alloys dics made using direct metal fabrication.* Medical Engineering & Physics, 2010. **32**: p. 645-652.

43. Van Bael, S., et al., *The effect of pore geometry on the in vitro biological behavior of human periosteum-derived cells seeded on selective laser-melted Ti6Al4V bone scaffolds.* Acta Biomaterialia, 2012. **8**(7): p. 2824-2834.

44. Weißmann, V., et al., *Comparison of Single Ti6Al4V Struts Made Using Selective Laser Melting and Electron Beam Melting Subject to Part Orientation.* Metals, 2017. **7**(3): p. 91.

45. Pakkanen, J., et al., *Study of Internal Channel Surface Roughnesses Manufactured by Selective Laser Melting in Aluminum and Titanium Alloys.* Metallurgical and Materials Transactions A, 2016. **47**(8): p. 3837-3844.

46. Gittens, R.A., et al., *The effects of combined micron-/submicron-scale surface roughness and nanoscale features on cell proliferation and differentiation.* Biomaterials, 2011. **32**(13): p. 3395-3403.

47. Faia-Torres, A.B., et al., *Differential regulation of osteogenic differentiation of stem cells on surface roughness gradients.* Biomaterials, 2014. **35**: p. 9023-9032.

48. Cheng, A., et al., *Additively maufactured 3D porous Ti-6Al-4V constructs mimic trabecular bone structure and regulate osteoblast proliferation, differentiation and local factor production in a porosity and surface roughnss dependent manner*. Biofabrication, 2014. **6**: p. 045007.

Figure Captions

Fig. 1. Repeating unit cell used in CAD

Fig. 2. OM images revealing the quality of SLM built TiTa alloys via in-situ alloying: (a) CP Ti (b) Ti10Ta (c) Ti30Ta and (d) Ti50Ta

Fig. 3. XRD patterns of SLM-built in-situ alloyed TiTa alloys with different Ta contents

Fig. 4. Line EDS analysis on Ti10Ta part: (a) Line EDS analysis across lath-α' boundary (b) Result of line EDS analysis

Fig. 5. SEM BSE images revealing the microstructure of SLM built TiTa alloys via in-situ alloying: (a) CP Ti (b) Ti10Ta (c) Ti30Ta and (d) Ti50Ta, with the right portion showing SE image (e) High magnification image of matrix region in Ti30Ta showing fine acicular-α'' phase (f) High magnification image of Ta poor region in Ti30Ta showing lath-α' phase (e) High magnification image of matrix region in Ti50Ta showing fine acicular-α'' phase (f) High magnification image of Ta poor region in Ti50Ta showing lath-α' phase. The red arrows highlight some of the tantalum-rich areas/un-melted tantalum

Fig. 6. EBSD mapping with IPF-Z colouring (BC showing minor phases): (a) CP Ti (IPF colouring for HCP), (b) Ti10Ta (IPF colouring for HCP and BC for un-melted Ta) , (c) Ti30Ta (IPF colouring for orthorhombic and BC for un-melted tantalum) , (d) Ti50Ta (IPF colouring for BCC and BC for HCP), (e) Low magnification BSE image of CP Ti, (f) Higher magnification EBSD mapping for Ti50Ta to highlight lath-α' phase. The white arrows highlight some of the tantalum-rich areas/un-melted tantalum

Fig. 7. Pole figure with in-plane axis parallel to the build direction (a) Ti (HCP) (b) Ti10Ta (HCP) (c) Ti30Ta (Orthorhombic) and (d) Ti50Ta (BCC).

Fig. 8. SEM BSE images revealing prior β grain nucleated from unmelted Ta particle

Fig. 9. Mechanical properties of titanium-tantalum alloys with different tantalum wt.% (a) Young modulus (b) ultimate tensile strength (c) yield strength and (d) percentage elongation

Fig. 10. Vickers microhardness value of TiTa alloys with different tantalum wt.% (a) x-y plane (b) y-z plane

Fig. 11. Fractography of (a) CP Ti (b) Ti10Ta (c)Ti30Ta (d)Ti50Ta

Fig. 12. Lattice structures for cell biocompatibility test (a) CAD model, (b) as-fabricated sample

Fig. 13. Relative cell number on cpTi, Ti6Al4V and TiTa lattice structures

Fig. 14. Florescence microscopy with live/dead kit for cpTi, Ti6Al4V and TiTa lattice structures

Table 1

Porosity and percentage unmelted Ta associated with each alloy composition

Alloy Composition	Porosity (%)	Unmelted Ta (%)
CP Ti	0.062	N/A
Ti10Ta	0.039	0.317
Ti30Ta	0.236	1.724
Ti50Ta	0.466	2.685

Table 2

Percentage Ta content of matrix region, phase(s) and lath/acicular width associated with each alloy composition in-situ alloyed with SLM. The phase(s) in majority are typed in bold

Alloy Composition	Ta Content in Matrix Region (Wt%)	Available Phase(s)	Lath/Acicular Width (µm)
CP Ti	N/A	**Lath α**	4.637
Ti10Ta	9.8	**Lath α'**, Un-melted Ta	3.279
Ti30Ta	29.1	**Acicular α''**, **Lath α'**, Un-melted Ta	0.079
Ti50Ta	47.6	**Equiaxed β**, **Acicular α''**, Lath α', Un-melted Ta	0.052

Table 3

Lattice constant of α and α’ martensite in Ti6Al4V

Phase	α	α’
Lattice Structure	HCP	HCP
Space Group	P63/mmc	P63/mmc
Lattice Constants	a = 0.295 nm	a = 0.293 nm
	c = 0.469 nm	c = 0.467 nm
Reference	[26]	[27]

Table 4

Porosity of the scaffolds

Material	**Porosity (%)**
TiTa	59.79 ± 0.68
Ti6Al4V	63.20 ± 0.55
cpTi	59.86 ± 0.59

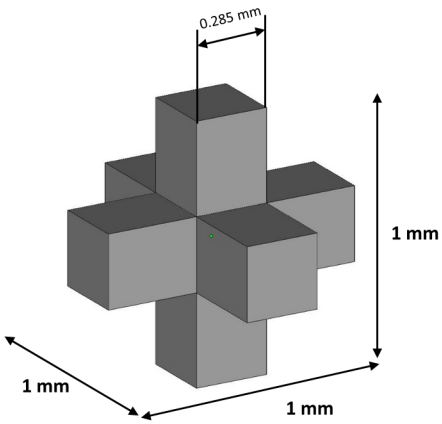

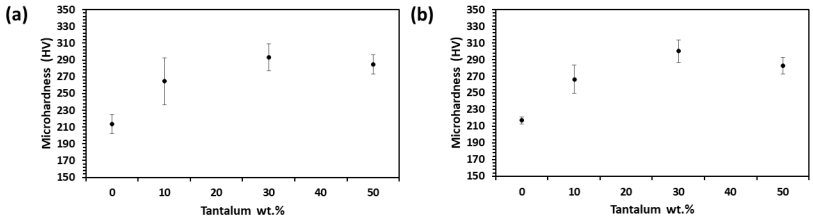

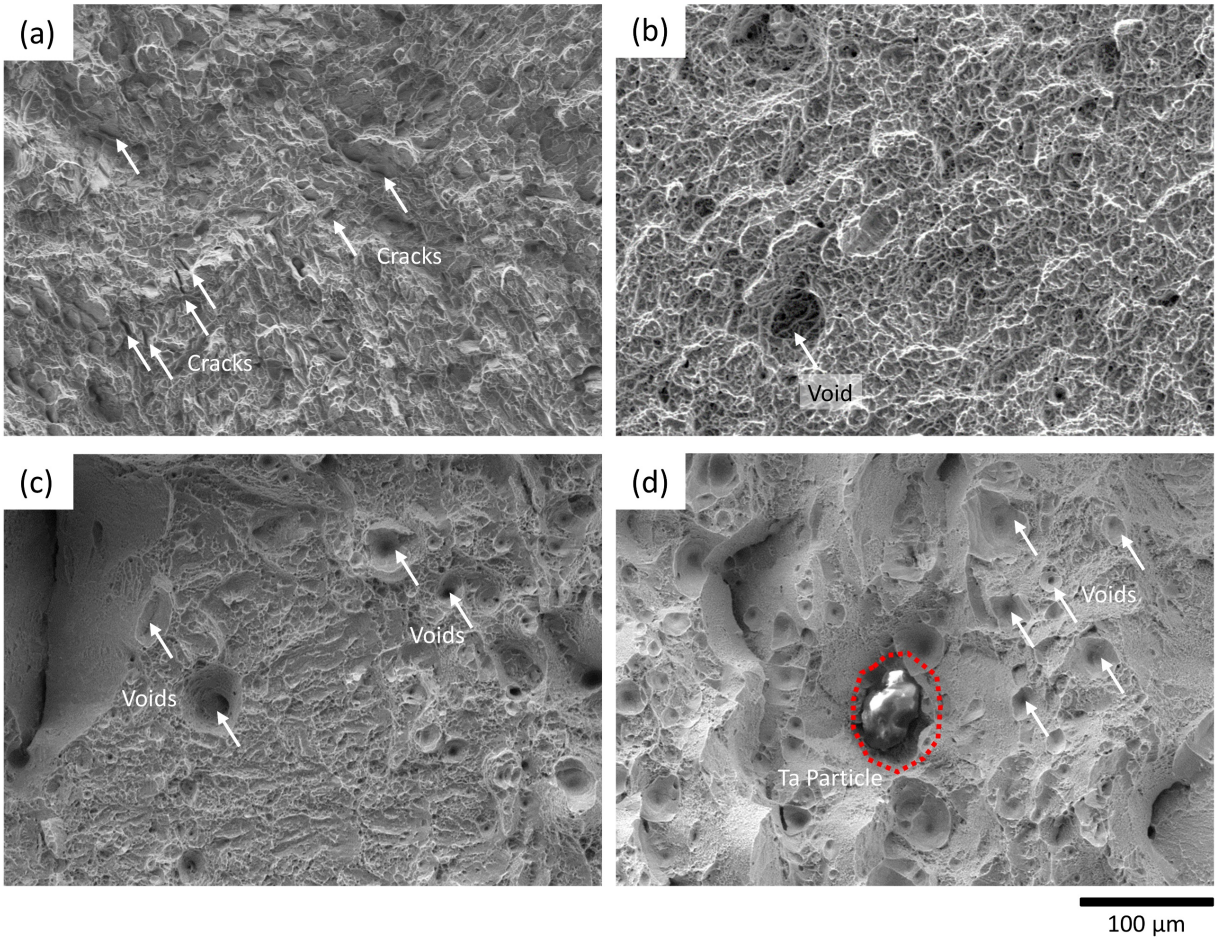
(a)
Cracks
Cracks
(b)
Void
(c)
Voids
Voids
(d)
Voids
Ta Particle
100 µm

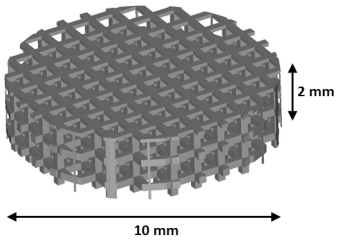

(a)

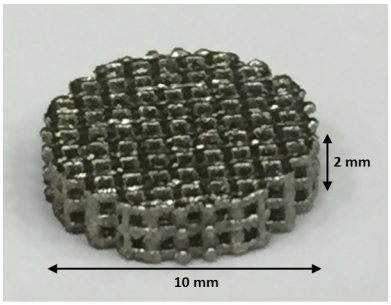

(b)

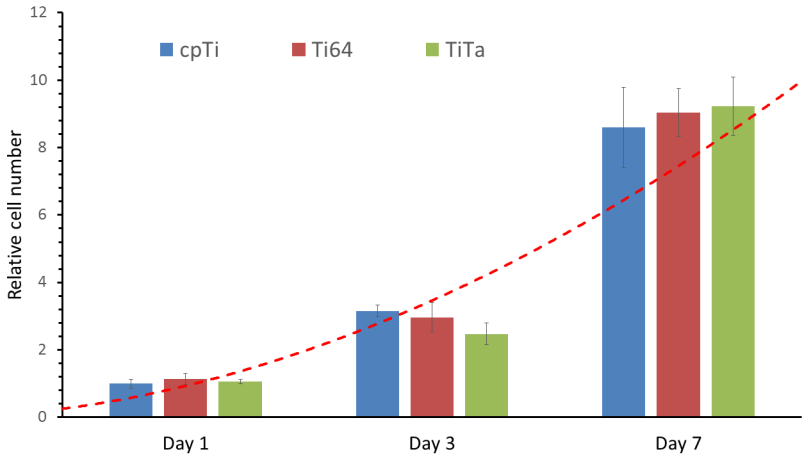

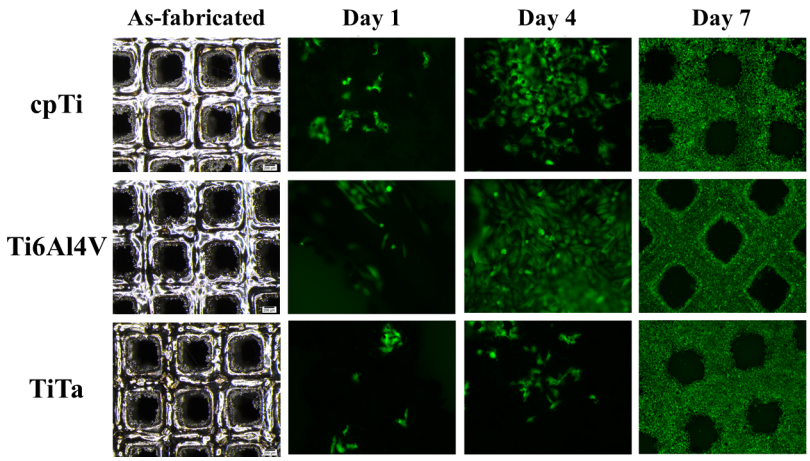

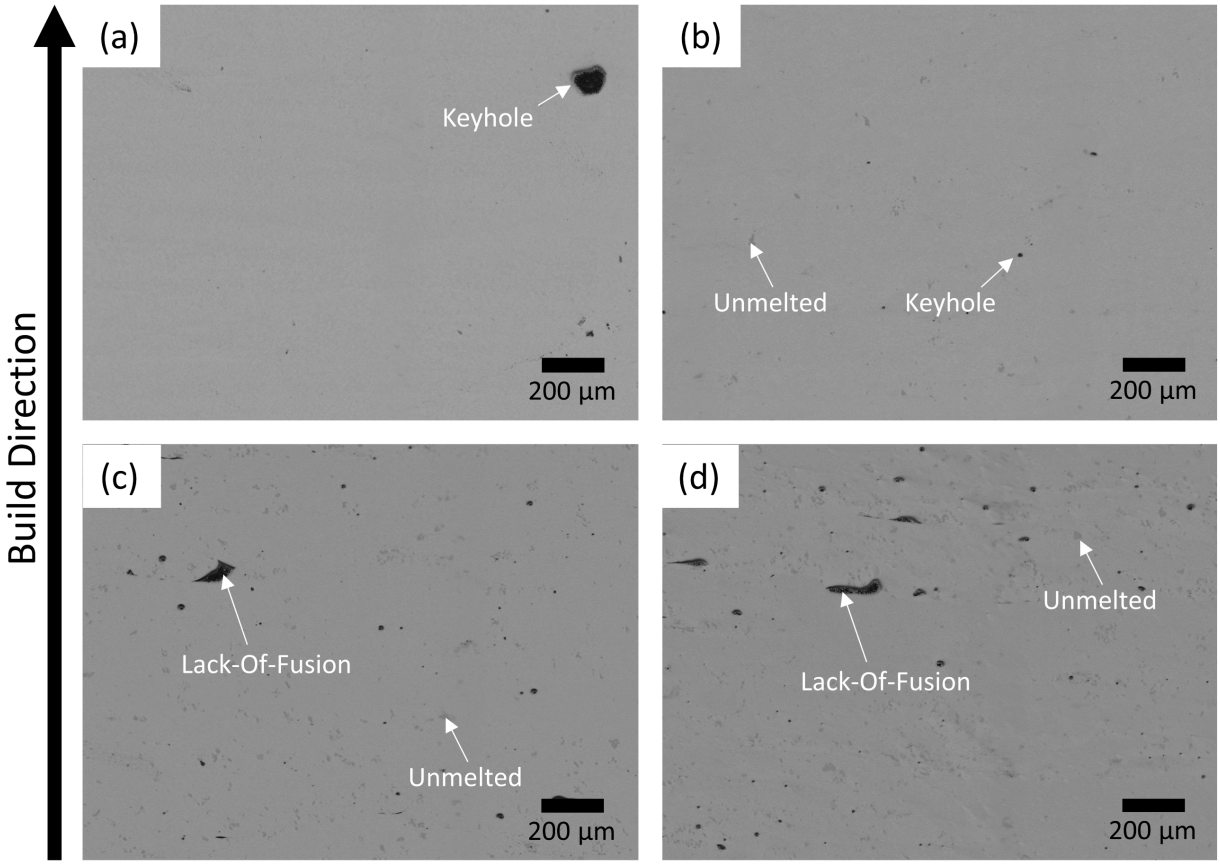
Build Direction
(a)
Keyhole
200 µm
(b)
Unmelted
Keyhole
200 µm
(c)
Lack-Of-Fusion
Unmelted
200 µm
(d)
Unmelted
Lack-Of-Fusion
200 µm

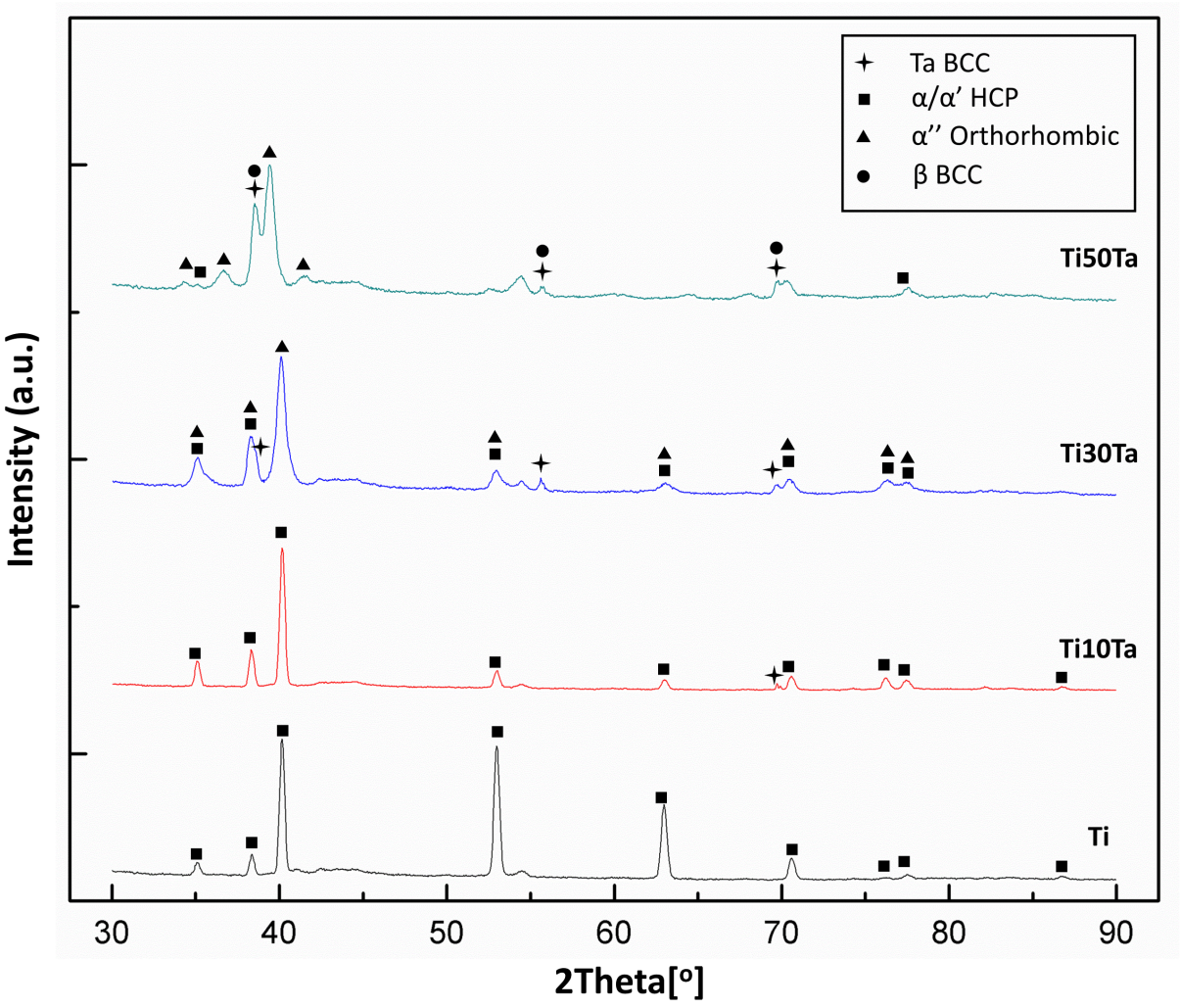
Ta BCC
α/α' HCP
α'' Orthorhombic
β BCC
Ti50Ta
Ti30Ta
Ti10Ta
Ti
Intensity (a.u.)
30
40
50
60
70
80
90
2Theta[°]

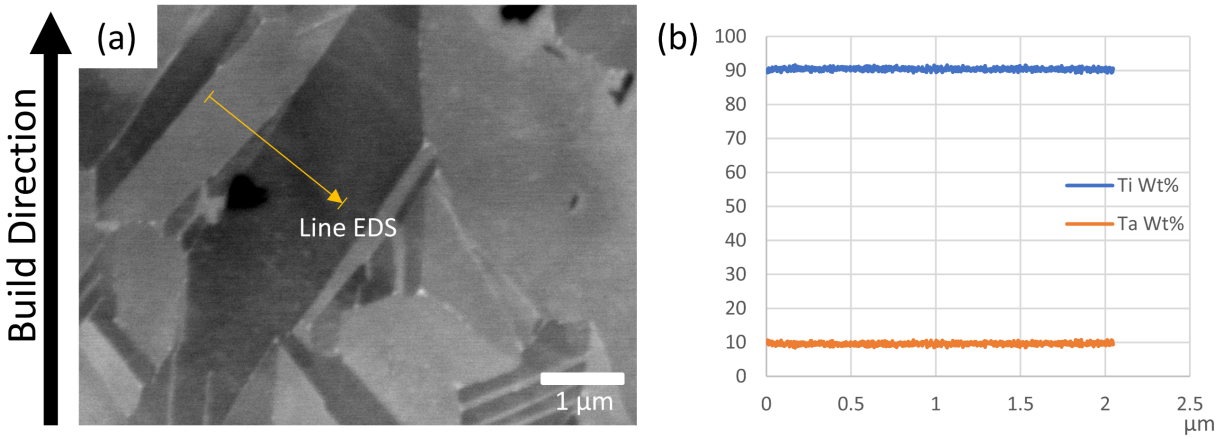

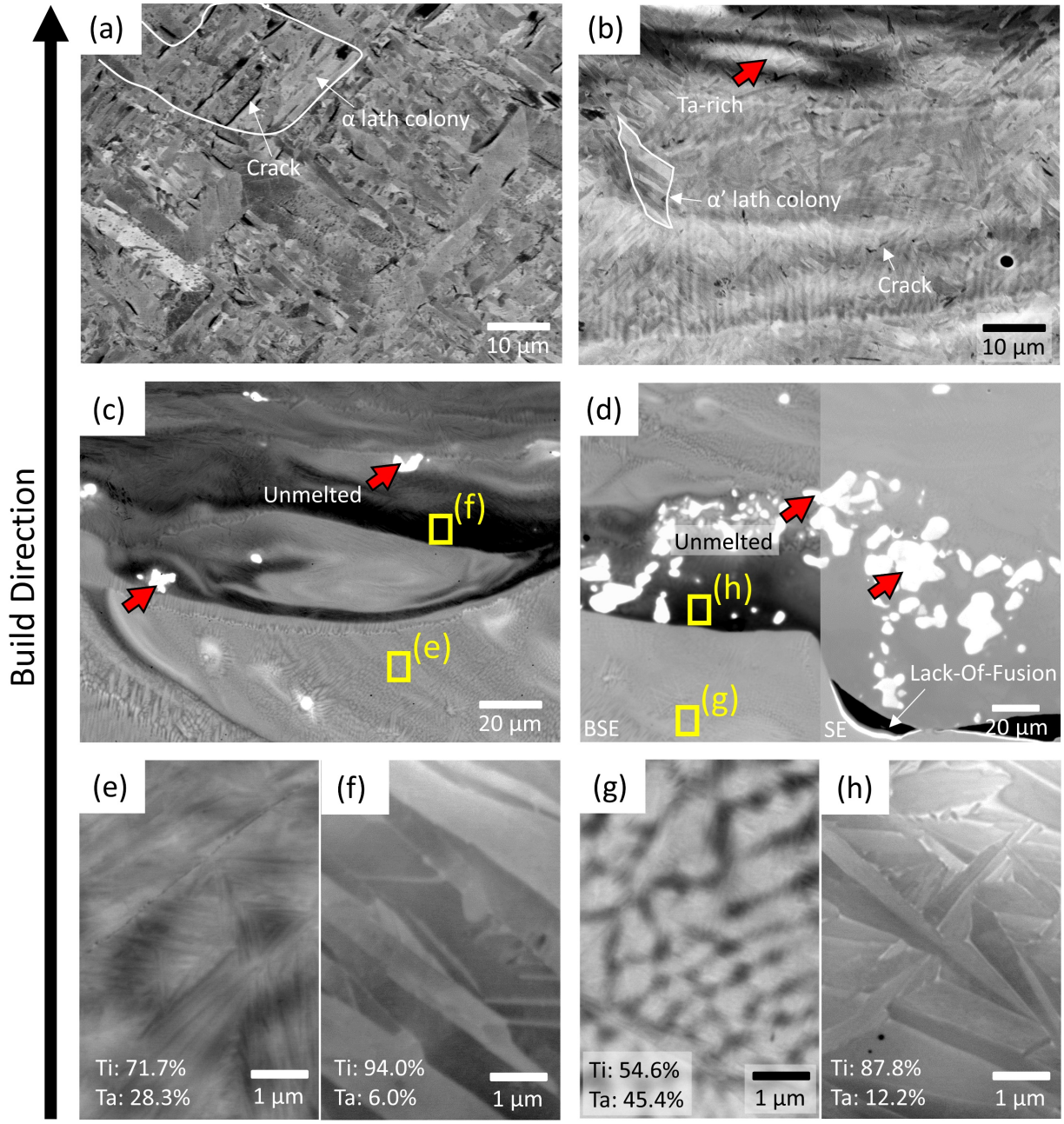
Build Direction
(a)
α lath colony
Crack
10 µm
(b)
Ta-rich
α' lath colony
Crack
10 µm
(c)
Unmelted
(f)
(e)
20 µm
(d)
Unmelted
(h)
(g)
BSE
SE
Lack-Of-Fusion
20 µm
(e)
Ti: 71.7%
Ta: 28.3%
1 µm
(f)
Ti: 94.0%
Ta: 6.0%
1 µm
(g)
Ti: 54.6%
Ta: 45.4%
1 µm
(h)
Ti: 87.8%
Ta: 12.2%
1 µm

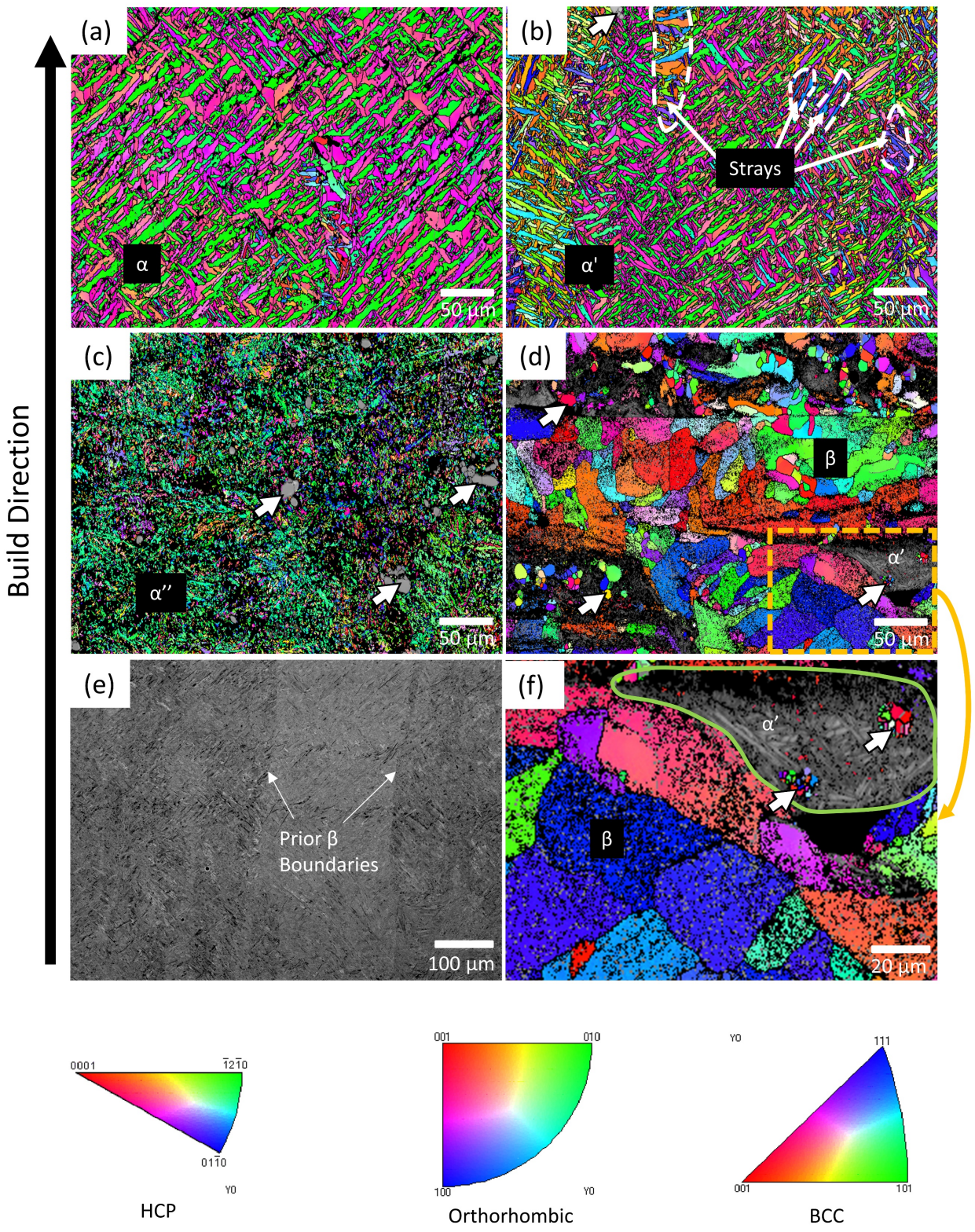
Build Direction
(a)
α
50 µm
(b)
Strays
α'
50 µm
(c)
α''
50 µm
(d)
β
α'
50 µm
(e)
Prior β
Boundaries
100 µm
(f)
α'
β
20 µm
0001
$\bar{1}2\bar{1}0$
$01\bar{1}0$
Y0
HCP
001
010
100
Y0
Orthorhombic
Y0
111
001
101
BCC

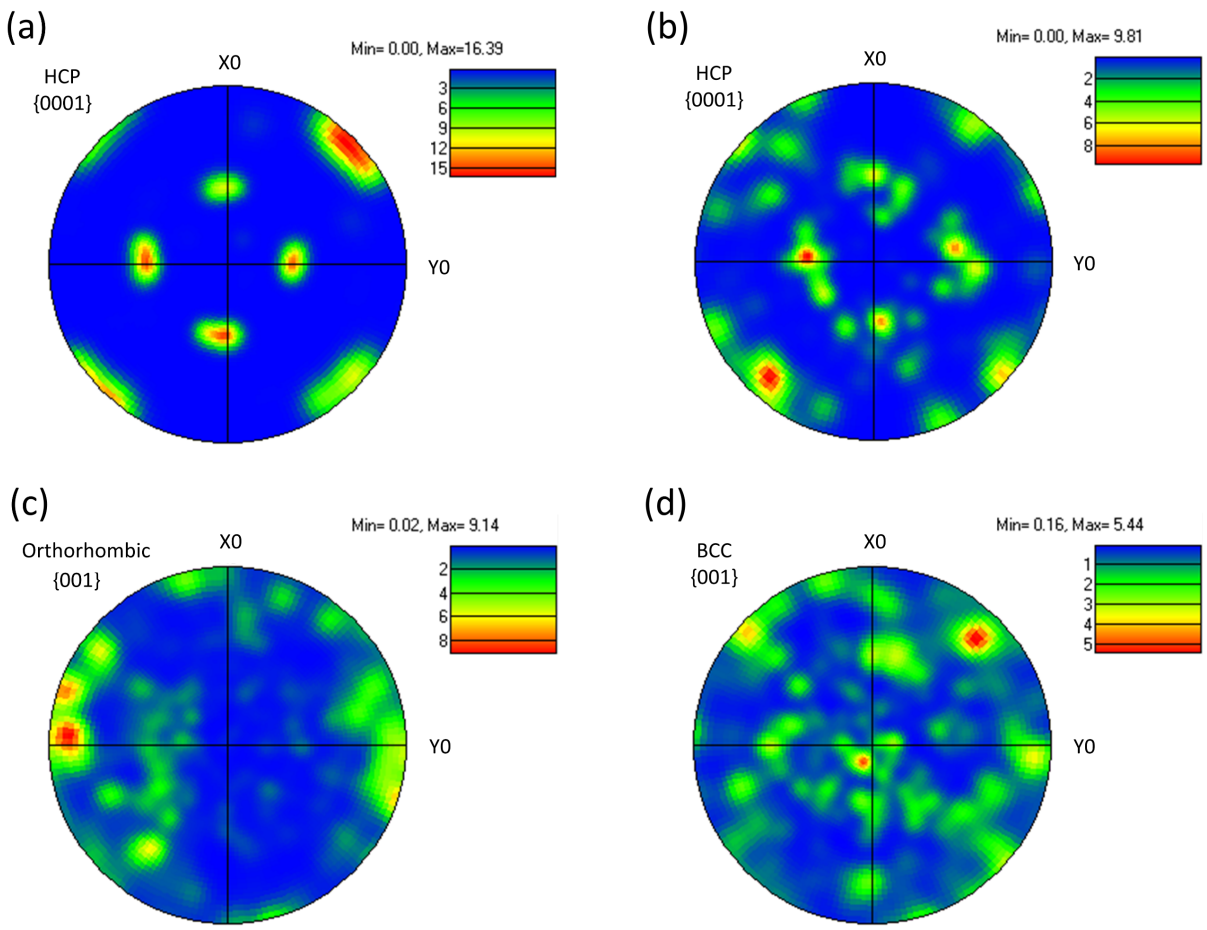
(a)
HCP
{0001}
X0
Y0
Min= 0.00, Max=16.39
3
6
9
12
15
(b)
HCP
{0001}
X0
Y0
Min= 0.00, Max= 9.81
2
4
6
8
(c)
Orthorhombic
{001}
X0
Y0
Min= 0.02, Max= 9.14
2
4
6
8
(d)
BCC
{001}
X0
Y0
Min= 0.16, Max= 5.44
1
2
3
4
5